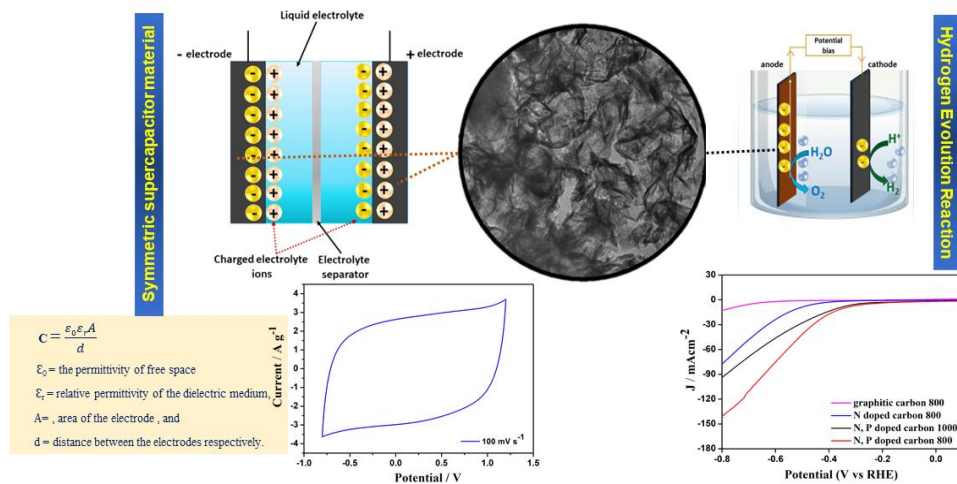# Chapter 5

Bi-functional hierarchically porous N, P co-doped reduced graphene oxide aerogel as a symmetric supercapacitor material and a robust hydrogen evolution reaction electrocatalyst

Symmetric supercapacitor material

Liquid electrolyte

− electrode   + electrode

Charged electrolyte ions   Electrolyte separator

$$C = \frac{\varepsilon_0 \varepsilon_r A}{d}$$

ε_0 = the permittivity of free space

ε_r = relative permittivity of the dielectric medium,

A= , area of the electrode , and

d = distance between the electrodes respectively.

Current / A g^{-1}

100 mV s^{-1}

Potential / V

Hydrogen Evolution Reaction

Potential bias

anode   cathode

H$_2$O   H$^+$

O$_2$ H$_2$

J / mAcm^{-2}

graphitic carbon 800
N doped carbon 800
N, P doped carbon 1000
N, P doped carbon 800

Potential (V vs RHE)

Key Highlights

❖ The synthesized N, P codoped RGO aerogel acts as an excellent symmetric supercapacitor.
❖ The working potential window of the capacitor can be extended up to 2V.
❖ The material delivers energy density with a value of 84 Wh kg^{-1}.
❖ The material is quite efficient to carry out hydrogen evolution reaction.

5.1 Introduction

In the past couple of decades, the world has developed at a breakneck pace. This fast-paced lifestyle, along with rapid population growth, is expected to continue for the foreseeable future, which in turn, has snowballed a huge demand for production, storage, and consumption of energy. People are moving from conventional technologies to portable electronic devices, electric vehicles, and smart grids, which has expedited the use of batteries and all-solid-state supercapacitors. Along with this shift, there comes new concerns related to energy production and storage, and environmental pollution. To find reliable and commercially viable solutions, researchers around the world have been working towards the development of novel electrode materials with special emphasis on their cost effectiveness, and their performance towards energy production, storage, and conversion devices.

In terms of energy sources, 82% of worldwide energy consumption is still reliant on the fossil fuels which in scarce supply. To move from the sole dependence on these fuels, there has been a huge push for alternative sustainable energy sources. During the last few decades, hydrogen has emerged as a potential clean energy source due to its sustainability, light weight and high energy density. Commercially, however, hydrogen is mostly produced by steam reforming process that uses fossil fuels. This is counter to our purpose. So, the alternate way, that is more preferable, is to produce hydrogen *via* electrochemical water splitting which produces zero by product, zero carbon emission, and also can be operated full-time without facing any concern for adverse weather conditions. However, it does face some critical challenges that need to be addressed before realizing the full commercial potential of the process. First and foremost is the electrocatalyst material. As we have mentioned previously several times Pt holds the best HER activity which needs to be supplanted by cost-effective, durable, and corrosion-resistant earth-abundant material. Carbon is the most abundant, low-cost and

---

This part of the thesis is communicated in:

Lahkar, S., Bora, A., Boruah, K., Puzari, P., and Dolui, S.K. Hierarchically porous N, P co-doped graphitic carbon as a symmetric supercapacitor material and a hydrogen evolution reaction electrocatalyst, *ACS Applied Energy Materials*.

a unique material which possesses high thermal and electrical conductivity, corrosion resistive property, hardness yet flexibility. In virtually all technologies, the use of carbon, in its many forms, is quite extensive [1-6]. In HER process also, a lot of research have been conducted with carbon nanomaterials. In 2014, some researchers used metal elements to modulate the density of electronic states of carbon and to reach the optimum H* adsorption free energy (ΔG(H*)) value on carbon surface [7,8]. Literature study reveals that optimized ΔG(H*) value can be achieved by doping with either metal atoms (Fe, Co, Cu, Mn, Mo, Ni, etc.) or non-metal atoms (N, P, B, etc.) [9-15]. Inspired by these studies, here we are trying to tune the electronic structure of carbon *via* non-metal doping for HER activity.

Concurrent to energy production, its storage, transportation, and conversion is also equally important. Due to the uneven geographic distribution of most of the sustainable energy resources, efficient and portable energy storage technologies with safety, environmental friendliness are required for their effective utilization. Carbon-based supercapacitors fulfill these demands in comparision to the lithium-based batteries as they impart metal independency, low cost, longer cycle life with no short circuit problem, shorter charge-discharge times and thus provide more power more swiftly [16]. Even though the overall fabrication process of a symmetric supercapacitor is relatively simple and cost effective, conventional carbon-based supercapacitors hold very low energy density that has drifted the interest of the researchers towards other avenues. Now, the charging-discharging process proceeds on the electrode/ electrolyte interface. Carbon supercapacitors, being electrical double layer capacitors (EDLCs), stores the energy by absorbing ions at this interface. Hence, another way to obtain an efficient carbon-based supercapacitor is to incorporate carbon in its three-dimensional form (graphene aerogel) that yields a high surface area and porous electrode [17]. Porosity helps in easy wettability of the electrode by the electrolyte, which causes quick charge/ discharge of the supercapacitor and high surface area assists to attain a high energy density by absorbing more ions. To further improve the capacitive behaviour, graphene aerogels are often doped by metallic (MnO_2, RuO_2, etc.) [18,19]and non-metallic (N, P, B, S, etc.) [14,15] species into the porous skeleton without destroying the original 3D matrix. It introduces structural defects and also changes the electronic distribution on the graphene surface to give a very high capacitive value.

In this work we have developed a metal free carbon-based material where N and P atoms are co-doped into the graphene aerogel network. The as synthesized material acts as an excellent symmetric supercapacitor material as well as an efficient HER electrocatalyst. The hierarchical porous nature as well as the dual doping attribute the overall enhanced performance of the material. The supercapacitor test has been carried out in three electrode and two electrode cells. To measure the supercapacitance property, we have carried out cyclic voltammetry (CV) tests, galvanostatic charge-discharge tests (GCD), electrochemical impedance spectral analysis. Further, the same material is applied as HER electrocatalyst and the material is capable to carry out HER efficiently. HER efficiency of the material has been examined by studying its polarization curve and Tafel plot. Durability and stability of the catalyst is assessed by chronoamperometry and cyclic voltammetry (CV) tests. The bifunctional property of the material establishes a scalable and cost-effective pathway for application of such catalysts in sustainable energy technologies providing another boost to dig into the study in this aspect further.

5.2 Materials and methods

5.2.1 Materials

All the required chemicals including graphite flakes, sodium nitrate ($NaNO_3$), potassium permanganate ($KMnO_4$), hydrogen peroxide (H_2O_2), sodium dodecyl sulfate (SDS), resorcinol, formaldehyde (HCHO), melamine, sodium hypophosphate (Na_3PO_4), sulphuric acid (H_2SO_4), hydrochloric acid (HCl) and Nafion were purchased from Sigma-Aldrich. They were of analytical reagent grade purity and were utilized directly.

5.2.2 Methods

5.2.2.1 Synthesis of graphene oxide (GO)

GO was synthesized using the conventional modified Hummers' method [20]. 1 g of graphite flakes and 0.5 g of $NaNO_3$ were mixed in a beaker. 23 mL of concentrated H_2SO_4 was poured under repeated stirring keeping the temperature below 20°C. After continually stirring the reaction mixture for an additional 2 h, 3 g of $KmnO_4$ was added slowly. Following that, the reaction was refluxed at 98°C for 12 h. The resulting sample solution was diluted by addition of 500 mL of distilled water. To ensure the complete

oxidation of $KmnO_4$, the mixture was treated with 5 mL of 10% H_2O_2. The obtained sample solution was then washed with dilute HCl and distilled water several times till the pH of the solution became 7. After that, the synthesized GO was filtered and dried in an oven.

5.2.2.2 Synthesis of N doped RGO aerogel

RGO aerogel was prepared by a method employed by Cheng *et al.* with slight modifications [21]. In a typical experiment, 1.23 g of resorcinol, 2 mg of Na_2CO_3, 0.2 g of melamine and 0.5 mL of HCHO were mixed together in a beaker and dissolved in 20 mL of deionized water to form a homogeneous solution by stirring. In another beaker, a dispersion of RGO (200 mg) was prepared in 10 mL of distilled water. 5 mg of SDS was added to it to ensure a homogeneous dispersion. After that, both the solutions were mixed under continuous stirring for an additional half hour. The solution was then completely sealed and the stirring was maintained at a speed of 50 rpm for 6 h. The temperature of the sample mixture was kept at 85°C for 12 h. Subsequently, the reaction mixture was shifted to an oven maintaining the temperature at 85°C for 3 days to obtain hydrogel. The gel was then washed with distilled water several times and freeze-dried, which finally yielded RGO aerogel. The as obtained aerogel was pyrolyzed at different temperatures (800°C, 900°C and 1000°C) under N_2 flow to obtain N doped RGO aerogel.

To synthesize our desired catalyst, i.e., porous N, P co-doped RGO aerogel, 1 g of N doped RGO aerogel, obtained in the previous step, was first mixed with 0.4 g of $Na_3PO_4.12H_2O$ which acts as P source. For a homogeneous mixture, a little bit of distilled water was used and then pyrolyzed at 600°C under N_2. In this work, we tried to optimize the catalytic performance of the composite by keeping the doping content constant while making the temperature parameter variable. After thermal activation at 600°C, the sample was washed with 0.1 M HCl to remove sodium ions. The sample was then dried and pyrolyzed at 800°C, 900°C and 1000°C under N_2 flow to get different samples.

5.2.3 Characterization and measurements

To understand the effect of N and P doping on the porous graphitic carbon network, XRD and FTIR spectra of the material was studied. The morphologies of sample were observed using FESEM, TEM. The composition of the present elements and their valence state was characterized by EDX and XPS. The electrochemical measurements were performed using the same equipment as we have mentioned in our previous chapters. Supercapacitor property of the catalyst was studied in both three-electrode and two-electrode cell systems. In the usual three-electrode system, a glassy carbon electrode with an area of about 0.07 cm^2 was drop-casted by the prepared catalyst (3 mg of the prepared catalyst dispersed in 0.1 mL of 0.5% Nafion solution) and air dried for direct use as the working electrode along with a Pt wire and an Ag/AgCl (in saturated KCl) electrode as the counter and the reference electrodes respectively. For the two-electrode system, two similar electrodes were prepared *via* drop-casting N, P co-doped RGO aerogel electrocatalyst on the 0.07 cm^2 surface area of glassy carbon electrode. 1 M Na_2SO_4 solution (for supercapacitor) or 0.5 M H_2SO_4 solution (for HER) was used as electrolyte. For HER, the electrochemical behaviour of the samples was studied using a standard three-electrode cell compartment.

5.3 Results and discussion

5.3.1 XRD analyses:
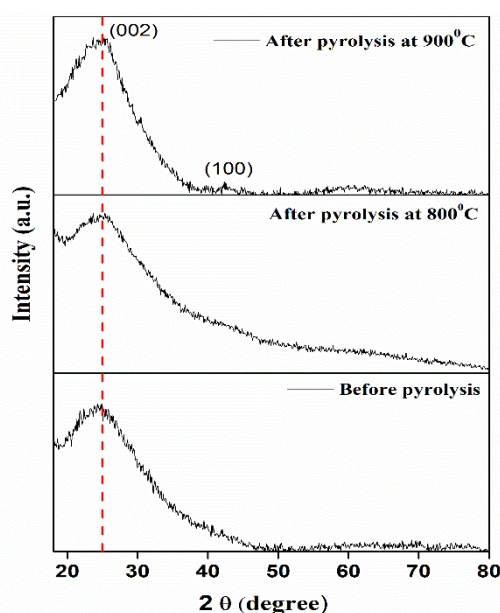
Figure 5.1 XRD patterns of N, P doped RGO aerogel i) before pyrolysis, pyrolysis at ii) 800^0C and at iii) 900^0C.

Figure 5.1 a) presents the XRD patterns of different samples collected to study the impact of pyrolysis temperature on the structure of the materials. In the XRD patterns of the pyrolyzed samples, two broad peaks at 2θ=~26° (002) and ~42.8° (100) coming out synchronously suggest graphitic nature in the material [23]. However, in case of unpyrolysed sample, the peak due to (100) plane is not observed may be due to presence of high concentration of impurity. The broadness of (100) peak after pyrolysis indicates the increase of the amorphous nature of the material. After pyrolysis of the sample at 800°C, a careful observation also indicates a slight shift of (002) plane towards the lower angle in N, P co-doped RGO aerogel. Understanding Bragg's law, λ=2dsinθ (where λ is the wavelength, d is the interlayer spacing and θ is the angle between the individual atomic planes), it is definite that the shifting interprets that the doping results in expansion of interlayer space due to introduction of some defect sites. This may be involved in modulation of surface electronic structure that favors the electrocatalytic performance. However, upon increasing pyrolysis temperature to 900°C, the peak corresponding to (002) plane shifts towards right indicating contraction of lattice. Nonetheless, the diffraction spectrum does not display any new peaks, indicating high purity of the synthesized catalyst.

5.3.2 BET analyses:
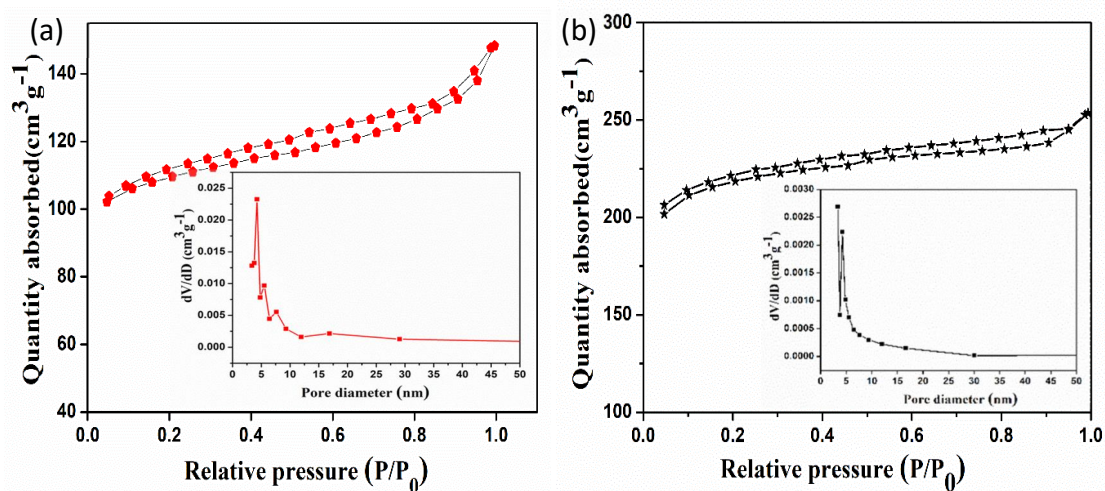
Figure 5.2 BET isotherms of (a) N doped RGO aerogel and (b) N, P co-doped RGO aerogel and the inset shows the corresponding pore size distribution curves.

To calculate the active surface area, nitrogen adsorption−desorption curves (BET isotherms) are acquired. BET isotherms of N doped RGO aerogel, and N, P co-doped RGO aerogel are presented in **Figure 5.2 (a)** and (**b**). Both the profile plots show a similar trend with a steep rise of the graph at the initial adsorption and a small hysteresis loop at $P/P_0 > 0.5$ indicates the presence of a large number of micropores and a few mesopores. Mesopores assist in the channelization of the ions and micropores provide a large number of active sites for ion adsorption. The specific surface area of N doped RGO aerogel is 307 m^2 g^{-1}. Notably, after N, P dual doping an overall increased specific surface area with a value of 609 m^2 g^{-1} can be acquired. This may be due to the structural change in the aerogel because of dual doping. Although P and N have the same valence electrons but P has a relatively larger atomic radius that causes a structural deformation of the hexagonal carbon skeleton. P-C bond length is more than the C-C bond length, resulting P stick out from the graphene plane. This increases the separation between the graphene layers and consequently, the surface area [22]. The aerogel formation makes the structure porous and the intercalating doping elements prevent the restacking of RGO sheets to a significant extent. The total pore volume of the synthesized catalysts N doped RGO aerogel and N, P co-doped RGO aerogel are 0.060 cm^3 g^{-1} and 0.049 cm^3 g^{-1} respectively. The Barrett−Joyner−Halenda (BJH) method is used to measure the pore size distribution of the materials. The inset of **Figure 5.2(a)** shows that the maximum pore size of N doped RGO aerogel is of 4.2 nm. The inset of **Figure 5.2(b)** shows that the majority of the pore size lies in the range of 2−15 nm. The maximum intensity peak of N, P co-doped RGO aerogel is centered at around 3.3 nm suggesting that maximum particles have pore size of lower than 3.5 nm. With increasing surface area, the size of the pores of N, P doped RGO aerogel significantly decreases.

5.3.3 RAMAN spectra analyses:

The graphitic structure and its electronic behaviour are studied *via* Raman spectra where two prominent bands are observed (**Figure 5.3**). The first band is the D band at 1381 cm^{-1} which is attributed to typical defects originating from the ring breathing mode vibration from sp^2 carbon rings primarily arising at the graphene edge [24,25]. The second band near about 1593 cm^{-1} is called the G band, which is attributed to the graphitic structure and correlated with the first-order scattering of E_{2g} phonon of sp^2 carbon atoms at the Brillouin zone center. Upon doping with N and P elements, the

I_D/I_G ratio increases from 0.8388 to 0.8496. This is because of the electron transfer from the elements with lone pair to the core element carbon of graphene suggesting modification of the band structure of graphene. The red shifting of frequency of the D band signifies an increased electron density of the N, P doped carbon due to which the lattice gets shielded and the interaction with nearby lattice is reduced. Upon incorporation of P, the intensity of D band rises which signifies increased structural defect. However, in both N doped carbon and N, P co-doped carbon materials, the lower I_D/I_G values than that of graphene signifies a high graphitization degree and hence increased electrical conductivity [26,27].
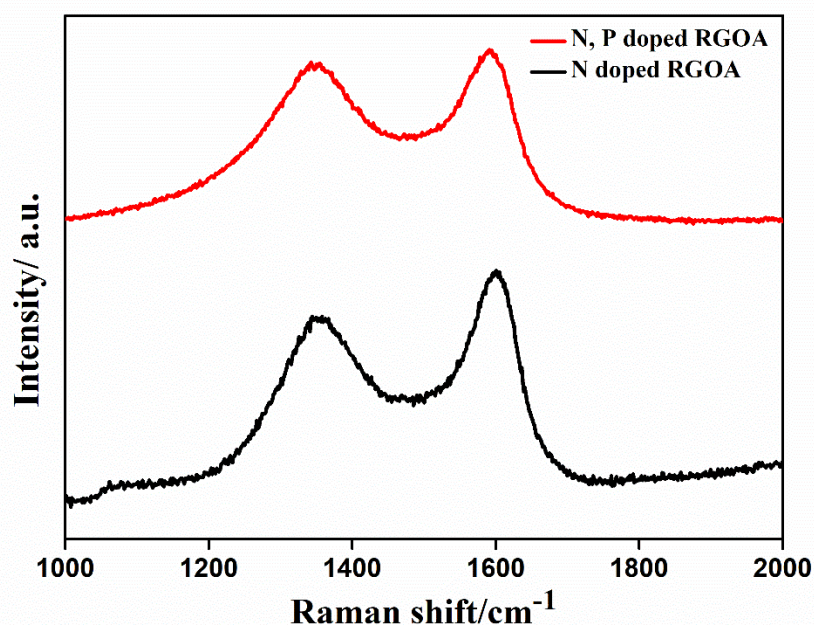
Figure 5.3 RAMAN spectra of N doped RGO aerogel 800 and N, P doped RGO aerogel 800.

5.3.4 X-ray photoelectron spectroscopy (XPS) analysis:

The elemental composition and its state in the synthesized final material N, P doped RGO aerogel was characterized by XPS. In high-resolution XPS spectrum (**Figure 5.4 (a)**) of C 1s, three distinguished peaks are fitted with binding energies of 284.3 eV, 285.2 eV and 286 eV which corresponds to C=C, C-C and C-N respectively. It represents the presence of both sp^2 and sp^3 carbon in the material [28]. The linear fitting of high-resolution N 1s spectra resolves the presence of three nitrogen peaks with

approximate binding energies of 398.4 eV, 401.3 eV and 403 eV attributed to pyridinic (N-6), pyrrolic (N-5) and quaternary nitrogen (N-Q) respectively (**Figure 5.4 (b)**) [29,30]. Both pyridinic and quaternary nitrogen provides extra electrons diminishing the hurdle of electron transfer barrier and thus enhances the conductivity of the material. The P 2p spectra has been resolved into 133.7 eV and 134.8 eV assigned to P-C and P-O respectively (**Figure 5.4 (c)**) [31]. Figure 2 (d) represents the survey spectra of the composite. The inset of Figure 2 (d) exhibits a prominent peak with the binding energy of ~ 531 eV which may be due to the presence of quinone in the composite [31]. Introduction of P element increases the conductivity and surface area of the material. The XPS spectra confirm the incorporation of P and N atoms with carbon structure without any individual cluster formation.
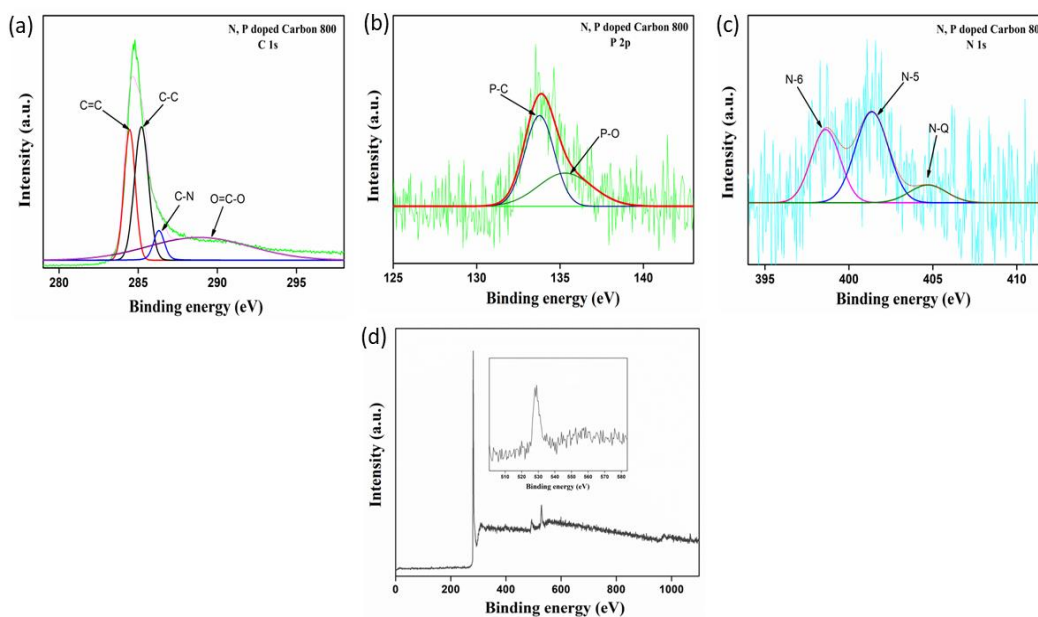

Figure 5.4 High-resolution XPS spectra of the elements (a) C, (b) P, (c) N in N, P co-doped RGO aerogel and (d) the survey spectra of N, P co-doped RGO aerogel along with the zoomed spectral region corresponding to the quinone region as the inset. N, P doped RGO aerogel 800.

5.3.5 SEM and EDX analyses:

Morphology of N, P doped RGO aerogel is interpreted by SEM images at different magnifications (**Figure 5.5 (a-c)**). SEM image clearly shows the porous surface of the

material which accelerates the diffusion of the electrolyte ions to the active surface. The morphology of the material is primarily responsible for excellent capacitance behavior and also functions as a better HER catalyst.
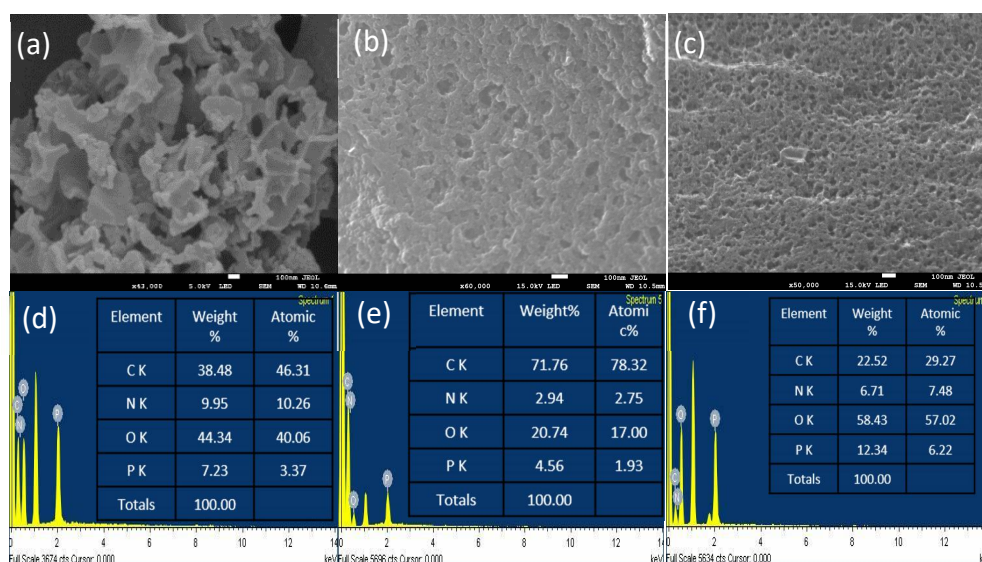

Figure 5.5 Morphological studies of N, P doped RGO aerogel (a-c) SEM images at different magnification, EDX spectra of N, P doped RGO aerogel at different temperatures (d) 600^0C, (e) 800^0C and (f) 1000^0C.

From the EDX spectra (**Figure 5.5 (d)-(f)**), the obtained weight percent ratio reveals that at 600^0C carbonization is not completed and a high amount of dopant concentration of N and P decreases the efficiency of the material both as supercapacitor and HER catalyst. After pyrolyzing at 800^0C the dopant elements are at a limited ratio to draw the maximum efficiency of the material. The presence of O is common due to immediate moisture adsorption on the material surface due to its porous nature. Upon increasing the pyrolysis temperature up to 1000^0C the core element carbon content drops to a great extent suggesting the collapse of graphitic structure which impacts the material performance negatively [32]. The EDX spectra display the presence of the required elements with negligible impurities.

5.3.6 TEM and SAED analysis:

In **Figure 5.6 (a,b)** TEM images confirm the interconnected 3D network of the aerogel which acts as the proper channel for both charge and mass transfer. At 10 nm range a large number of mesopores are visible in the structure (**Figure 5.6 (c)**). SAED pattern represents well-defined concentric rings corresponding to (002) and (100) plane of RGO (**Figure 5.6 (d)**).
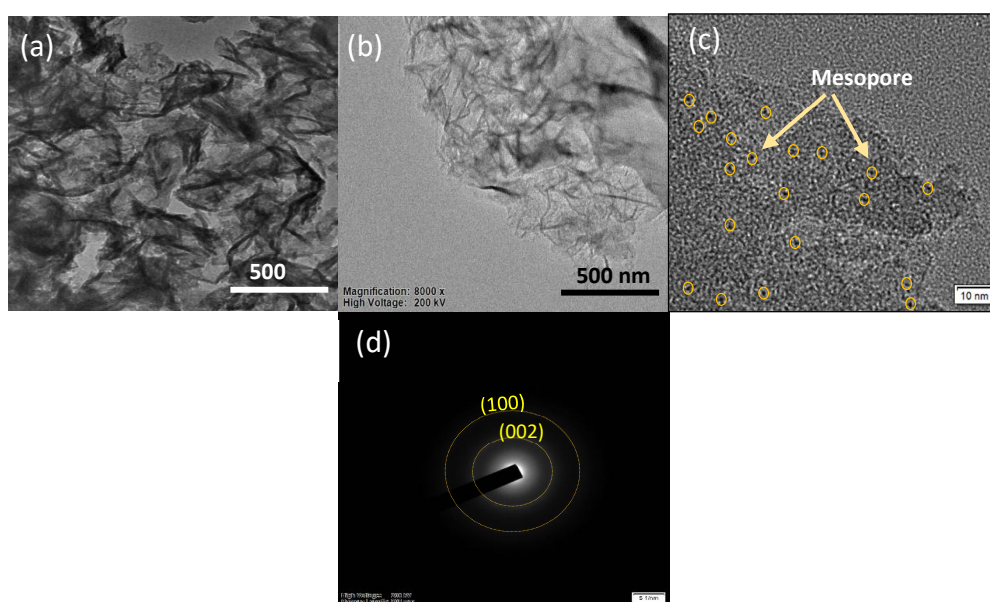

Figure 5.6 TEM images of N, P doped graphitic carbon at low resolution (a-b) and at high resolution (c) showing the presence of a large number of mesopores, (d) SAED pattern represents the planes corresponding to (100) and (002) plane.

5.3.7 Supercapacitor performance of N, P co-doped RGO aerogel

For the best performance of a supercapacitor, a highly conductive material is extremely desirable. Increased charge transfer through the electrode maintains a high-rate capability by lowering electrochemical resistance (ESR). Another requirement is having maximum surface area with controlled porosity. In case of EDLCs, the charges are accumulated at the electrode's surface or near it so that the ions move around into the pores to a form double layer just at the right rate, thus a large accessible surface area is favored. Graphite-based materials possess all these properties making them ideal candidate for application in supercapacitors.

5.3.7.1 N, P co-doped RGO aerogel as electrode material in supercapacitors
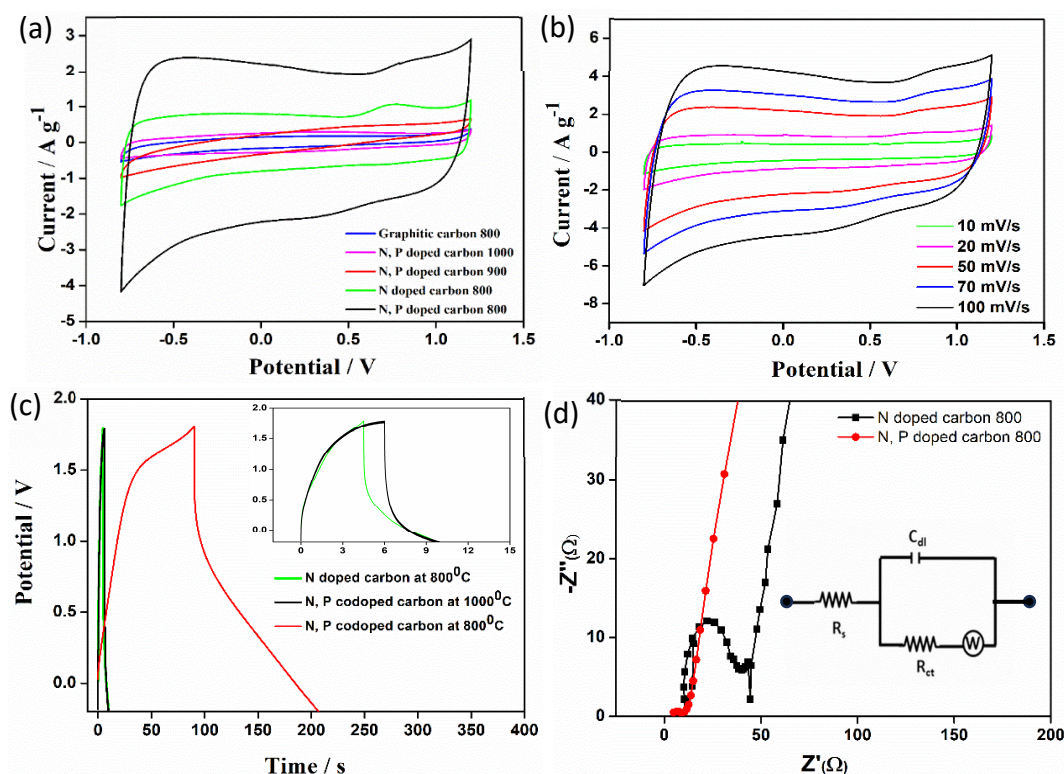
Figure 5.7 (a) CV curves of the different electrode materials in a three-electrode configuration at a scan rate of 50 mV sec^{-1}, (b) the CV curves of N, P co-doped RGO aerogel at different scan rates, (c) charge-discharge tests of the synthesized materials at a current density of 10 A g^{-1}, and (d) electrochemical impedance spectra of N doped RGO aerogel and N, P co-doped RGO aerogel electrodes in a three-electrode cell fitted with an equivalent circuit as shown in the inset of (d).

The electrochemical performances of the materials were analyzed *via* CV using a three-electrode system in 1 M Na$_2$SO$_4$ solution at a scan rate of 50 mV sec^{-1}. The performance variation of the synthesized catalysts was monitored with the help of voltammograms by varying the parameters like doping and pyrolysis temperature. CV profiles for different synthesized catalysts are displayed in **Figure 5.7 (a)**, where the curves present a rectangular shape with slight humps specifying the co-existence of EDLC as well as faradic pseudo-capacitance. Acquired XPS analysis data confirms the presence of the quinone group in our composite which undergoes redox reaction upon receiving electrons from the material. The increase in the rate of redox reaction predominantly depends on the

electrons provided by the material surface. N, P codoped RGO aerogel-800 delivers maximum electrons and hence shows superior capacitance compared to other synthesized catalysts.
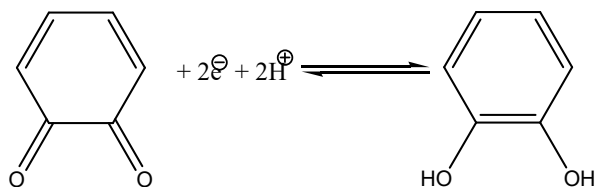
The steepness of the CV profile near -0.8 V and +1.2 V region is due to the high current density which represents low electrochemical resistance of the electrode. The most probable reason is the porous nature of the material which doesn't impede the flow of electrolyte ions to reach the electroactive surface. After N doping, there occurs a dramatic increase in capacitance. Upon N incorporation, both in the graphitic edges and the basal plane, it becomes easier for the lone pair of electrons present on N to interact with the electrolyte resulting in an increase in the capacitance *via* pseudo-capacitive effect [33,34,35]. P atom, on the other hand, bond predominantly with graphitic edges of carbon, which increase the surface area, pore volume, and wettability of the catalyst, thus facilitating additional interaction between the electrolyte and the catalyst's electroactive surface. Dual doping also has an effect on the overall increase of the working potential. N and P co-doping disrupt the charge neutrality of C atom creating new charge sites (P^+ upon P doping and C^+ upon N doping) together with structural defect sites [36]. Overall, the synergistic effect of N, P co-doping with the well-interconnected 3D porous aerogel network greatly enhances the super-capacitive property of the material. Upon P doping, the CV area of the catalyst is enhanced and it is almost twice as that of N doped RGO aerogel pyrolyzed at 800°C. From the graph, it is obvious that the best performance is obtained with N, P co-doped RGO aerogel pyrolyzed at 800°C for 2 h. Carbonization temperature of 800°C is found to be the optimum temperature for supercapacitance performance. Beyond that, the pyrolysis temperature has detrimental effect. At temperatures below 800°C, the carbonization process is not complete and the presence of more N and P content decreases the electrical conductivity and rate performance, whereas increasing carbonization temperature

decreases the efficiency of the material. This may either be due to the high temperature being too prohibitive to disrupt its porous nature or due to the thermal decomposition of core element C causing the collapse of some of the hexagonal rings leading to disruption of its graphitic structure. The perfect quasi-rectangular shape of the cyclic voltammograms of the catalyst at the potential range from -0.8 V to 1.2 V represents the adequacy of its use as both cathode and anode in aqueous electrolyte.

Upon increasing the scan rate, the shape of the CV curves remains indistinguishable along with increased current density and the integrated surface area perfectly claims ideal supercapacitance property (**Figure 5.7 (b)**). Beyond the potential range of -0.8 V to 1.2 V, there occurs an immediate rise of the curve signifying oxygen and hydrogen evolution. Hence the specific potential window is bounded in this region for all the capacitance tests. A significant disadvantage of using graphene is that the potential window along with the capacitance area drops rapidly mainly due to the stacking of graphene layers that leaves the pore size too small to be approached by the electrolyte ions. This, however, does not transpire in the porous network of our material which prevents restacking while providing proper channels for the electrolyte ions to reach the electrode surface [37,38].

The performance of the supercapacitor was studied by GCD analysis between -0.8 V to 1.2 V (**Figure 5.7 (c)**). The GCD analysis data for the synthesized catalysts show an analogous increasing trend as that of the CV data. Among the prepared materials N, P co-doped RGO aerogel exhibits the longest discharging time that represents the best capacitance property. The catalyst delivers a specific capacitance (C_{sp}) value of 596 F g^{-1} in a three-electrode system.

The EIS measurement was carried out and evaluated against a corresponding equivalent circuit to probe the resistance of the materials (**Figure 5.7 (d)**). Semicircles are observed in the high frequency region from 100 kHz-10 Hz. Upon introduction of the electrode to the electrolyte, the electrode-electrolyte interface offers some resistance which is the solution resistance (R_S) or ESR, the values of which are 9.4 and 3.7 Ω for N doped RGO aerogel and N, P co-doped RGO aerogel respectively, both pyrolized at 800°C. A lower R_S value indicates the enhanced power density and rate capability of the material. After electrode-electrolyte interaction, the ions are absorbed on the electrode

surface and diffuse through the surface to reach the bulk of the material which provides charge transfer resistance (R_{CT}) that manifests in a semicircle [39,40]. In case of N, P co-doped RGO aerogel, the R_{CT} value is lower than that of N-doped RGO aerogel. In the mid frequency region, a $45°$ slope signifies a typical Warburg impedance corresponding to the transportation of ions to the inner pore surface of the active electrode material. A more vertical line is representative of the ideal capacitive behaviour of the material [41]. Both N doped RGO aerogel and N, P co-doped RGO aerogel display a straight tail indicating that rapid diffusion of ions augments the electrical double layer formation at low frequencies. N and P co doping not only reduces R_S, but also R_{CT} and Warburg impedance values. Decrease in these values clearly denotes that the 3D networked hierarchical porous structure of the synthesized catalyst and doping with both N and P atom greatly ease ion diffusion to the active site generating the electrochemical double layer. Also, the doping increases the conductivity and wettability of the electrode material.

### 5.3.7.2 Performance of N, P co-doped RGO aerogel as symmetric supercapacitor
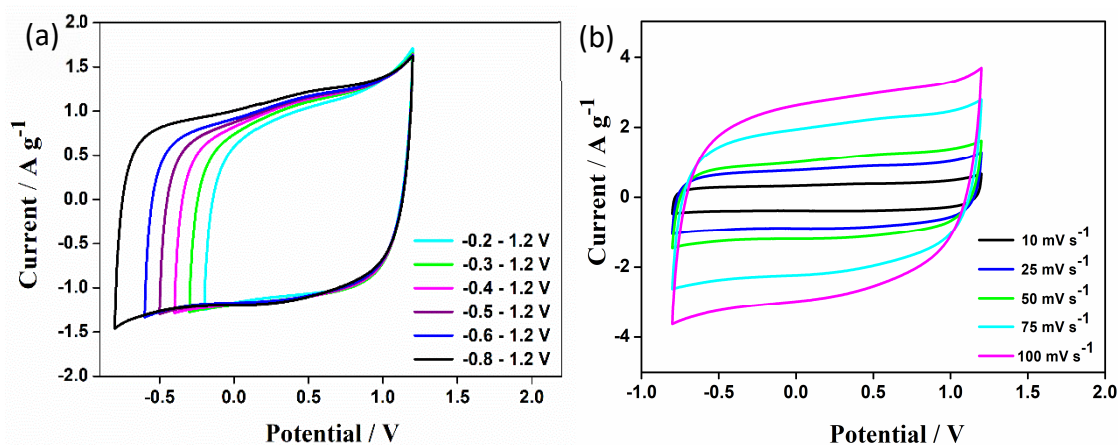
Figure 5.8 (a) CV at different potential windows from (-0.2 V to 1.2 V) to (-0.8 V to 1.2 V) at a scan rate of 50 mV sec^{-1}, (b) CV at different scan rates (from inner to outer: 10, 25, 50, 70 and 100 mV s^{-1}).

In the three-electrode cell system, the super-capacitive nature of the synthesized carbon-based composites has been checked. The obtained results of supercapacitors are extended by performing the capacitor experiments in a two-electrode cell system. Total

cell voltage can be regarded as the sum of the overall positive and negative potential. Thus, the working potential window can be extended up to 2V. As shown in **Figure 5.8 a)**, monitoring the behaviour of the symmetric cell at different potential windows at a scan rate of 50 mV s^{-1}display fine EDLC supercapacitor behaviour of rectangular voltammograms. The rectangular shape remains consistent upon increase in scan rates (**Figure 5.8 (b)**).
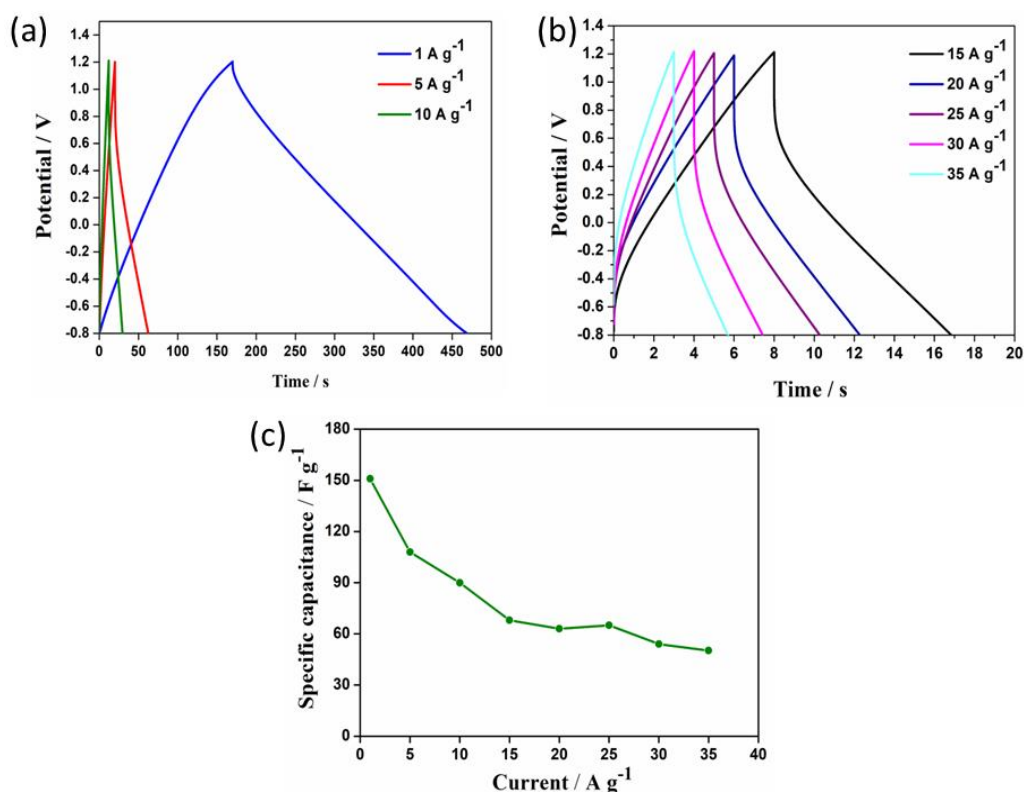
Figure 5.9 (a) charge-discharge tests at different current densities: 1, 5, 10 A g^{-1}, (b) charge-discharge tests at higher current densities: 15, 20, 25, 30 and 35 A g^{-1}, (c) variation of calculated C$_{sp}$ with current density.

The charging/ discharging ability of the symmetric capacitor was tested with GCD curves at different current densities in **Figure 5.9 (a)** and **(b)**. Moderately symmetrical triangular shape of the curves implies a fast and reversible reaction [42]. From the GCD graph at 1 A g^{-1}, the calculated C$_{sp}$ value obtained is 152 F g^{-1}. The symmetrical nature of the GCD curves remains stable even at high current density suggesting perfect rate capability and reversibility of the device. Upon a 10-fold rise in current density from 1 A g^{-1} to 10 A g^{-1}, almost 72% of the capacitance retention is observed (**Figure 5.9 (c)**).

The low capacitance at high current density may be the limited diffusion time for the electrolyte ions to get into the active pore sites.
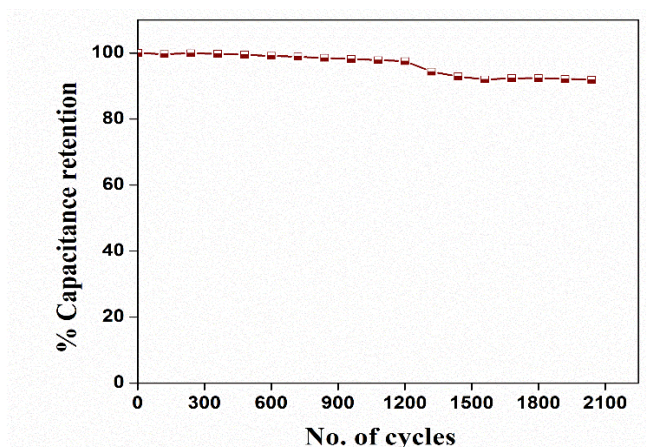
Figure 5.10 Performance of the device during 2000 cycles of the catalyst N, P doped RGO aerogel in two electrode cell measurements.

The durability of the capacitor material was checked via cycling stability in **Figure 5.10**. The supercapacitor retains almost 92% of its capacitance after 2000 CV cycles manifesting outstanding cycle stability.
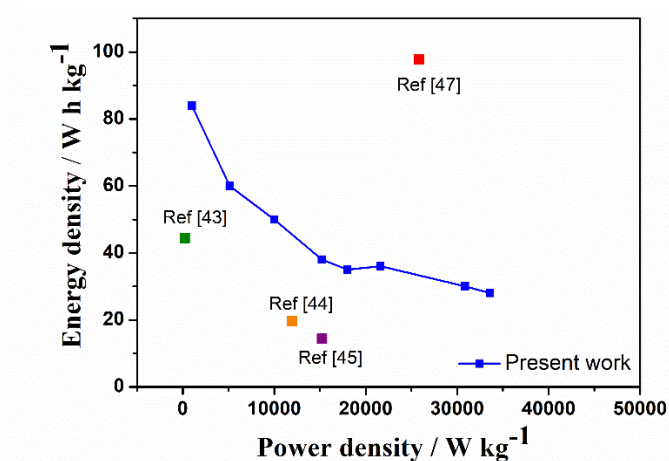
Figure 5.11 Ragone plot of N, P co-doped RGO aerogel as symmetric supercapacitor for its performance comparison with other carbon-based supercapacitors.

To analyze the symmetric super-capacitive performance of our cell with previous studies encompassing graphene composites, a plot was projected with energy density *vs.* power density which is called the Ragone plot (**Figure 5.11**). The symmetric

supercapacitor used in this study manifests a peak energy density of 84 W h kg^{-1} at a power density of 1.001 kW kg^{-1}. An ultimate power density of 33.6 kW kg^{-1} can be withdrawn at an energy density of 28 W h kg^{-1}. Because of the porous nature of the electrode material, the electrolyte temporarily inserts in the pores and slowly releases the ions that extend the charge discharging time leading to the increase of energy density. This performance can beat numerous carbon-based supercapacitors because of the high surface area, controlled porosity, and the mechanical permanence of the 3D graphitic network. The obtained values are compared with the formerly reported values of symmetric supercapacitors in Table 5.1. The energy density, power density, and stability of the supercapacitor material make it viable for possible commercial use. It is even safer than most commercial supercapacitors due to the use of aqueous electrolyte.

Table 5.1 Comparision of the performances of different carbon-based symmetric supercapacitors

SSC electrode material	cell voltage	P$_{max}$ (kW kg^{-1})	Electrolyte	W$_{max}$ (Wh kg^{-1})	Cycle stability (capacitance retention)	Reference
P doped carbon wood	1.2V	0.437	6 M KOH	41.2	90.5% after 10000 cycles	[43]
N doped carbon /Carbon paper	1 V	12.3	PVA/KOH gel	17.5	87.6% after 20000 cycles	[44]
N doped carbon /Graphene	1.8 V	15.126	6 M KOH	12.7	96.6% after 10000 cycles	[45]
Activated carbon	1.6 V	-	0.5 M Na$_2$SO$_4$	10	76% after 10000 cycles	[46]
Porous carbon with carbon dots	2.6 V	26	1.5 M Na$_2$SO$_4$	107.5	97.2% after 5000 cycles	[47]
N doped carbon nanosheet	2 V	50	2 M Li$_2$SO$_4$	27.2	90.1% after 2000 cycles	[48]
N doped activated carbon	1.5 V	0.0389	0.1 M H$_2$SO$_4$/PVA	8.6	65% after 50000 cycles	[49]
N, O codoped carbon nanosphere	3.5 V	17.5	6 M KOH	80.3	96.5% after 10000 cycles	[50]
Porous carbon from silkworm excrement	2.8 V	6.473	LiPF$_6$	138.4	77.8% after 8000 cycles	[51]
O, N, S doped activated carbon	1.8 V	14	1 M NaClO$_4$	21.48	98% after 10000 cycles	[52]
Porous carbon with numerous N and O functional groups	1 V	10.5	PVA/KOH sol	9.67	90.2% after 10000 cycles	[53]
N, S co-doped porous carbon fiber film	0.8 V	2.402	PVA/KOH gel	16.35	79.7% after 10000 cycles	[54]
N, P doped porous graphitic carbon	2V	33.6	1 M Na$_2$SO$_4$	84	92% after 2000 cycles	This work

Effect of temperature on the performance of symmetric supercapacitor:
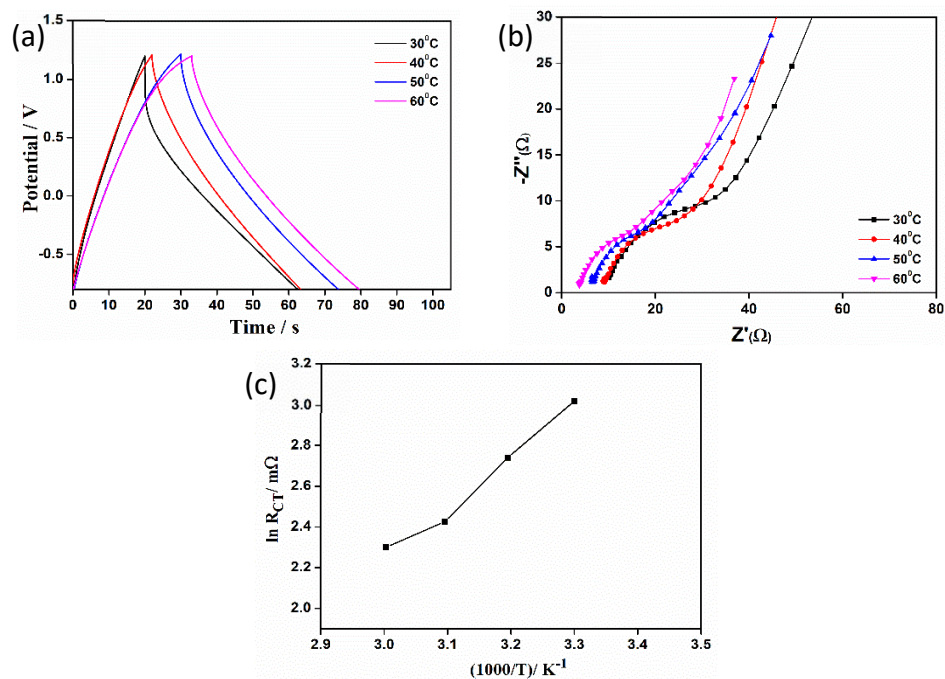
Figure 5.12 (a) GCD curves of the supercapacitor at different operating temperatures from 40°C to 60°C at a current density of 5 A g^{-1}, (b) EIS at different working temperatures and (c) variation of R$_{CT}$ of the supercapacitor with temperature.

For the use of the supercapacitor in the practical field, it is quite important that it functions at a broader spectrum of temperatures (40, 50, and 60°C). The C$_{sp}$ values of the devices were measured with temperature increment. Upon increasing temperature, both charging and discharging times increase (**Figure 5.12 (a)**). The effect of temperature on the performance parameters was also studied *via* the Nyquist plot of the device at different working temperatures (**Figure 5.12 (b)**). Obviously, the R$_{S}$ value decreases with increasing temperature, courtesy of the increase in ion mobility. Also, the decrease of R$_{CT}$ value upon increasing temperature implies surface modification by increased wettability of the electrode material thus easing the diffusion of electrolyte on the bulk of the electrode surface (**Figure 5.12 (c)**).

5.3.8 Electrocatalytic activity of N, P co-doped RGO aerogel in HER

Apart from the application of N, P co-doped RGO aerogel as an efficient supercapacitor material, the material was also tested as a catalyst for HER. To obtain information on the HER activity of the prepared catalyst, electrochemical characterization was performed in a three-electrode set-up at ambient temperature. 0.5 M H_2SO_4 solution is used as the electrolyte in the evaluation of catalytic performance for HER.
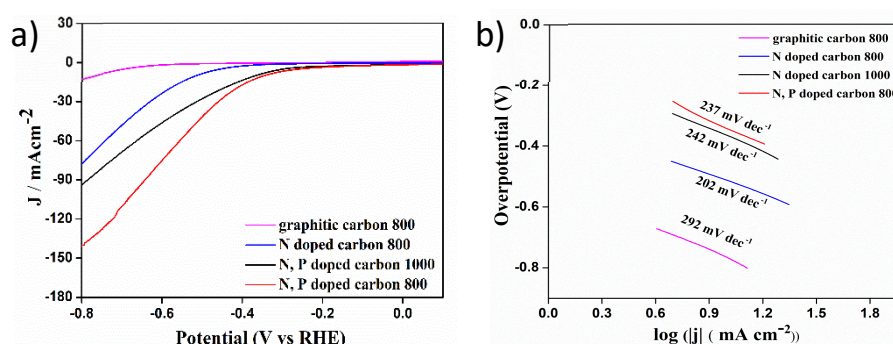
Figure 5.13 Electrocatalytic performances of the catalysts in 0.5 M H_2SO_4 in terms of their a) polarization curves and b) Tafel plots.

The polarization curves (J-V plots) were obtained by sweeping the potential from 0 to -0.8 V (*vs* Ag/AgCl) with a sweeping rate of 50 mV sec^{-1}. In this investigation, all the potentials were measured with standard calomel electrode (SCE) and then converted to reversible hydrogen electrode (RHE) using the equation 5.1.

$$E(RHE) = E(SCE) + 0.0591 \text{ pH} + 0.1976 \text{ V} \qquad \text{equation 5.1}$$

From the non-zero cathodic current measurements (**Figure 5.13 (a)**), it is observed that N, P co-doped RGO aerogel pyrolyzed at 800°C exhibits better catalytic efficiency for HER than the other prepared catalysts. The catalyst requires -0.351 V overpotential (η_{10}) to achieve the benchmark current density of 10 mA cm^{-2} which is considerably smaller than that of N, P co-doped RGO aerogel pyrolyzed at 1000°C (-0.373 V), N doped RGO aerogel pyrolyzed at 800°C (-0.516 V) and graphitic RGO aerogel (-0.77 V) with the equivalent catalyst loading. It is noteworthy that after N and

P atoms are doped concurrently in the carbon structure, the catalytic efficiency greatly increases. According to the Sabatier principle, $\Delta G(H^*)$ value should neither be too strong nor too weak to pinpoint a good HER catalyst. From electronegativity viewpoint, C is more electronegative than P and less electronegative than N. Thus, N attracts the sp^2 electrons toward itself and P atom pushes its own electrons towards C. Thus, there occurs a channel of electron transfer *via* C atom. N, P co-doping not only breaks the electro-neutrality of the sp^2 C rings but also modulates its charge density. Moreover, because of the presence of P, electron density on C becomes high. Hence, a strong binding of H_{ads} occurs on the surface of C. But since N atom is also present, it attracts the electron density towards itself assisting in the desorption process. Due to this, a perfect balance for H atom adsorption-desorption is achieved on C atoms allowing it to catalyze the HER. Furthermore, the presence of P atoms could effectively inhibit the electro-oxidation of active catalytic carbon sites [55].

To find out the mechanistic pathway of HER, Tafel slopes are obtained in **Figure 5.13 (b)** by fitting the linear portion of polarization curve data to equations 3.1 a) and b). N, P co-doped RGO aerogel pyrolyzed at 800°C shows a Tafel slope value of 237 mV dec^{-1} that is lower than that of N, P doped RGO aerogel pyrolyzed at 1000°C (242 mV dec^{-1}), N doped RGO aerogel pyrolyzed at 800°C (202 mV dec^{-1}) and graphitic RGO aerogel (292 mV dec^{-1}) (**Figure 5.13 (b)**). Smaller Tafel slope hints faster HER kinetics as well as lower demands of activation energy for H_2 evolution. Tafel slope analysis shows that the HER kinetics is likely governed by Volmer-Heyrovsky mechanism and removal of H_2 from H_2O molecule on the surface of the electrode (Volmer step) is the rate determining step. The possible HER mechanism on N, P co-doped RGO aerogel is as follows:

$$H_3O^+(aq) + e^- + C^* \rightarrow CH_{ads} + H_2O \qquad \text{(Volmer step)}$$

$$CH_{ads} + H_3O^+(aq) + e^- \rightarrow H_2(g) + H_2O(l) + C^* \qquad \text{(Heyrovsky step)}$$

C^* and H_{ads} stand for the active carbon sites and the adsorbed hydrogen on the active sites respectively.

The stability of the catalyst N, P doped RGO aerogel pyrolyzed at 800°C was checked by performing 1000 CV scans within the potential range from 0.1 V to -0.7 V (*vs* RHE) with a scan rate of 50 mV s^{-1} in 0.5 M H_2SO_4 solution. The performance of the catalyst remains almost constant before and after the stability (**Figure 5.14 (a)**).
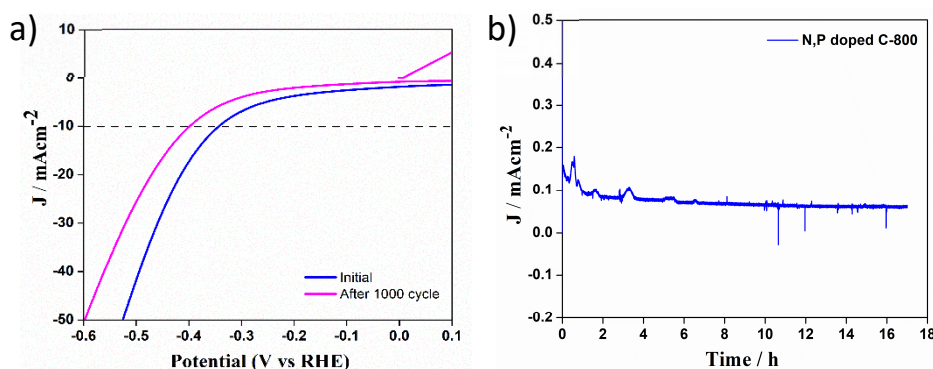
Figure 5.14 a) electrochemical stability of N, P co-doped RGO aerogel as measured from CV profiles recorded at 50 mV s^{-1} upto 1000 cycles and b) time dependence study at an overpotential of 100 mV in 0.5 M H_2SO_4.

Furthermore, long-term functional strength of the catalyst was verified by carrying out chronoamperometric (CA) analysis. The CA profile of N, P co-doped RGO aerogel pyrolyzed at 800°C in **Figure 5.14 (b)** is not smooth due constant H_2 bubble generation on the electrode surface. Chronoamperogram for ~17 h at -60 mV *vs* RHE overpotential affirms the excellent stability and durability of the catalyst.

5.4 Conclusion

In summary, N, P codoped RGO aerogel was synthesized by an easy multistep route with an enhanced capacitance ability, energy density as well as improved electrocatalytic activity towards HER. The outstanding supercapacitance ability of the material is specifically attributed to the morphology and increased wettability of the material. N, P co-doped RGO aerogel exhibited an ultimate energy density of 84 W h kg^{-1} at a power density of 1.001 kW kg^{-1} in aqueous electrolyte. The material also exhibited a wide working potential range of 2V and can be operated at a broad range of temperatures. The same material also efficiently catalyzes the HER at 0.351 V vs RHE to acquire the standard current density of 10 mA cm^{-2} and shows stability upto 17 hr without any degradation of current density. The increased conductivity and synergistic effect from dual doping break

the electroneutrality of carbon and prompted its activity both as a supercapacitor as well as a HER electrocatalyst. However, it is noteworthy that pyrolyzation temperature does play an efficient role in tuning the efficiency of the material.

5.5 References

1] Yoo, E., Kim, J., Hosono, E., Zhou, H.S., Kudo, T., and Honma, I. Large reversible Li storage of graphene nanosheet families for use in rechargeable lithium ion batteries. *Nano letters*, *8*(8):2277-2282, 2008.

2] Wang, X., Zhi, L., and Müllen, K. Transparent, conductive graphene electrodes for dye-sensitized solar cells. *Nano letters*, *8*(1):323-327, 2008.

3] Eda, G., Fanchini, G., and Chhowalla, M. Large-area ultrathin films of reduced graphene oxide as a transparent and flexible electronic material. *Nature nanotechnology*, *3*(5):270-274, 2008.

4] Shao, Y., Wang, J., Wu, H., Liu, J., Aksay, I.A., and Lin, Y. Graphene based electrochemical sensors and biosensors: a review. *Electroanalysis: An International Journal Devoted to Fundamental and Practical Aspects of Electroanalysis*, *22*(10):1027-1036, 2010.

5] Machado, B.F. and Serp, P. Graphene-based materials for catalysis. *Catalysis Science & Technology*, *2*(1):54-75, 2012.

6] Hadjizadeh, A. and Doillon, C.J. Directional migration of endothelial cells towards angiogenesis using polymer fibres in a 3D co-culture system. *Journal of tissue engineering and regenerative medicine*, *4*(7):524-531, 2010.

7] Zou, X., Huang, X., Goswami, A., Silva, R., Sathe, B.R., Mikmeková, E., and Asefa, T. Cobalt-embedded nitrogen-rich carbon nanotubes efficiently catalyze hydrogen evolution reaction at all pH values. *Angewandte Chemie*, *126*(17):4461-4465, 2014.

8] Deng, J., Ren, P., Deng, D., Yu, L., Yang, F., and Bao, X. Highly active and durable non-precious-metal catalysts encapsulated in carbon nanotubes for hydrogen evolution reaction. *Energy & Environmental Science*, *7*(6):1919-1923, 2014.

9] Bayatsarmadi, B., Zheng, Y., Vasileff, A., and Qiao, S.Z. Recent advances in atomic metal doping of carbon-based nanomaterials for energy conversion. *Small*, *13*(21):1700191, 2017.

10] Nagy, B., Ábrahám, D., Dobos, G., Madarász, J., Onyestyák, G., Sáfrán, G., Geissler, E., and László, K. Molybdenum doped carbon aerogels with catalytic potential. *Carbon*, *66*:210-218, 2014.

11] Hu, S., Qu, X., Li, P., Wang, F., Li, Q., Song, L., Zhao, Y., and Kang, X. Photocatalytic oxygen reduction to hydrogen peroxide over copper doped graphitic carbon nitride hollow microsphere: the effect of Cu (I)-N active sites. *Chemical Engineering Journal*, *334*:410-418, 2018.

12] Zhang, J., Fan, C., Zhao, W., and Zang, L. Improving bio-H_2 production by manganese doped magnetic carbon. *International Journal of Hydrogen Energy*, *44*(49):26920-26932, 2019.

13] Redlich, P., Loeffler, J., Ajayan, P.M., Bill, J., Aldinger, F., and Rühle, M. B☐ C☐ N nanotubes and boron doping of carbon nanotubes. *Chemical physics letters*, *260*(3-4):465-470, 1996.

14] Yaglikci, S., Gokce, Y., Yagmur, E., and Aktas, Z. The performance of sulphur doped activated carbon supercapacitors prepared from waste tea. *Environmental Technology*, *41*(1):36-48, 2020.

15] Nasini, U.B., Bairi, V.G., Ramasahayam, S.K., Bourdo, S.E., Viswanathan, T., and Shaikh, A.U. Phosphorous and nitrogen dual heteroatom doped mesoporous carbon synthesized via microwave method for supercapacitor application. *Journal of Power Sources*, *250*:257-265, 2014.

16] Shukla, A.K., Sampath, S., and Vijayamohanan, K. Electrochemical supercapacitors: Energy storage beyond batteries. *Current science*, *79*(12):1656-1661, 2000.

17] Qian, H., Kucernak, A.R., Greenhalgh, E.S., Bismarck, A., and Shaffer, M.S. Multifunctional structural supercapacitor composites based on carbon aerogel modified high performance carbon fiber fabric. *ACS applied materials & interfaces*, *5*(13):6113-6122, 2013.

18] Lv, H., Yuan, Y., Xu, Q., Liu, H., Wang, Y.G., and Xia, Y. Carbon quantum dots anchoring MnO_2/graphene aerogel exhibits excellent performance as electrode materials for supercapacitor. *Journal of Power Sources*, *398*:167-174, 2018.

19] Zhang, J., Ding, J., Li, C., Li, B., Li, D., Liu, Z., Cai, Q., Zhang, J., and Liu, Y. Fabrication of novel ternary three-dimensional RuO_2/graphitic-C_3N_4@ reduced graphene oxide aerogel composites for supercapacitors. *ACS Sustainable Chemistry & Engineering*, *5*(6):4982-4991, 2017.

[20] Paulchamy, B., Arthi, G., and Lignesh, B.D. A simple approach to stepwise synthesis of graphene oxide nanomaterial. *J Nanomed Nanotechnol*, *6*(1):1, 2015.

[21] Cheng, W.Y., Wang, C.C., and Lu, S.Y. Graphene aerogels as a highly efficient counter electrode material for dye-sensitized solar cells. *Carbon*, *54*:291-299, 2013.

[22] Nie, G., Deng, H., Huang, J., and Wang, C. Phytic acid assisted formation of phosphorus-doped graphene aerogel as electrode material for high-performance supercapacitor. *International Journal of Electrochemical Science*, *15*(12):12578-12586, 2020.

[23] Hidayah, N.M.S., Liu, W.W., Lai, C.W., Noriman, N.Z., Khe, C.S., Hashim, U., and Lee, H.C. Comparison on graphite, graphene oxide and reduced graphene oxide: Synthesis and characterization. *AIP conference proceedings*, 1892:150002, 2017.

[24] Liu, J., Li, Q., Zou, Y., Qian, Q., Jin, Y., Li, G., Jiang, K., and Fan, S. The dependence of graphene Raman D-band on carrier density. *Nano letters*, *13*(12):6170-6175, 2013.

[25] Tuinstra, F. and Koenig, J.L. Raman spectrum of graphite. *The Journal of chemical physics*, *53*(3):1126-1130, 1970.

[26] Gao, S., Tang, Y., Wang, L., Liu, L., Sun, Z., Wang, S., Zhao, H., Kong, L., and Jia, D. Coal-based hierarchical porous carbon synthesized with a soluble salt self-assembly-assisted method for high performance supercapacitors and Li-ion batteries. *ACS Sustainable Chemistry & Engineering*, *6*(3):3255-3263, 2018.

[27] Dutta, S., Ray, C., Sarkar, S., Pradhan, M., Negishi, Y., and Pal, T. Silver nanoparticle decorated reduced graphene oxide (rGO) nanosheet: a platform for SERS based low-level detection of uranyl ion. *ACS applied materials & interfaces*, *5*(17):8724-8732, 2013.

[28] Niu, F., Yang, J., Wang, N., Zhang, D., Fan, W., Yang, J., and Qian, Y. $MoSe_2$-covered N, P-doped carbon nanosheets as a long-life and high-rate anode material for sodium-ion batteries. *Advanced Functional Materials*, *27*(23):1700522, 2017.

[29] Wei, W., Chen, Z., Zhang, Y., Chen, J., Wan, L., Du, C., Xie, M., and Guo, X. Full-faradaic-active nitrogen species doping enables high-energy-density carbon-based supercapacitor. *Journal of Energy Chemistry*, *48*:277-284, 2020.

[30] Li, X.X., Zhu, P.Y., Li, Q., Xu, Y.X., Zhao, Y., and Pang, H. Nitrogen-, phosphorus-doped carbon–carbon nanotube CoP dodecahedra by controlling zinc content for high-performance electrocatalytic oxygen evolution. *Rare Metals*, *39*(6):680-687, 2020.

[31] Zhang, J., Qu, L., Shi, G., Liu, J., Chen, J., and Dai, L. N, P-codoped carbon networks as efficient metal-free bifunctional catalysts for oxygen reduction and hydrogen evolution reactions. *Angewandte Chemie*, *128*(6):2270-2274, 2016.

[32] Fu, H.H., Chen, L., Gao, H., Yu, X., Hou, J., Wang, G., Yu, F., Li, H., Fan, C., Shi, Y.L., and Guo, X. Walnut shell-derived hierarchical porous carbon with high performances for

electrocatalytic hydrogen evolution and symmetry supercapacitors. *International journal of hydrogen energy*, *45*(1):443-451, 2020.

[33] Wang, D.W., Li, F., Yin, L.C., Lu, X., Chen, Z.G., Gentle, I.R., Lu, G.Q., and Cheng, H.M. Nitrogen-doped carbon monolith for alkaline supercapacitors and understanding nitrogen-induced redox transitions. *Chemistry–A European Journal*, *18*(17):5345-5351, 2012.

[34] Ornelas, O., Sieben, J.M., Ruiz-Rosas, R., Morallon, E., Cazorla-Amorós, D., Geng, J., Soin, N., Siores, E., and Johnson, B.F. On the origin of the high capacitance of nitrogen-containing carbon nanotubes in acidic and alkaline electrolytes. *Chemical Communications*, *50*(77):11343-11346, 2014.

[35] Yuan, W., Zhou, Y., Li, Y., Li, C., Peng, H., Zhang, J., Liu, Z., Dai, L., and Shi, G. The edge- and basal-plane-specific electrochemistry of a single-layer graphene sheet. *Scientific reports*, *3*(1):2248, 2013.

[36] Chen, H., Sun, F., Wang, J., Li, W., Qiao, W., Ling, L., and Long, D. Nitrogen doping effects on the physical and chemical properties of mesoporous carbons. *The Journal of Physical Chemistry C*, *117*(16):8318-8328, 2013.

[37] Liu, C., Yu, Z., Neff, D., Zhamu, A., and Jang, B.Z. Graphene-based supercapacitor with an ultrahigh energy density. *Nano letters*, *10*(12):4863-4868, 2010.

[38] Ke, Q. and Wang, J. Graphene-based materials for supercapacitor electrodes–A review. *Journal of Materiomics*, *2*(1):37-54, 2016.

[39] Chen, L.F., Zhang, X.D., Liang, H.W., Kong, M., Guan, Q.F., Chen, P., Wu, Z.Y., and Yu, S.H. Synthesis of nitrogen-doped porous carbon nanofibers as an efficient electrode material for supercapacitors. *ACS nano*, *6*(8):7092-7102, 2012.

[40] Dong, S., He, X., Zhang, H., Xie, X., Yu, M., Yu, C., Xiao, N., and Qiu, J. Surface modification of biomass-derived hard carbon by grafting porous carbon nanosheets for high-performance supercapacitors. *Journal of Materials Chemistry A*, *6*(33):15954-15960, 2018.

[41] Bard, A.J., Faulkner, L.R., and White, H.S. *Electrochemical methods: fundamentals and applications*. John Wiley & Sons, 2022.

[42] Cheng, J., Lu, Z., Zhao, X., Chen, X., and Liu, Y. Green needle coke-derived porous carbon for high-performance symmetric supercapacitor. *Journal of Power Sources*, *494*:229770, 2021.

[43] Wang, F., Cheong, J.Y., He, Q., Duan, G., He, S., Zhang, L., Zhao, Y., Kim, I.D., and Jiang, S. Phosphorus-doped thick carbon electrode for high-energy density and long-life supercapacitors. *Chemical Engineering Journal*, *414*:128767, 2021.

[44] Yan, B., Feng, L., Zheng, J., Zhang, Q., Dong, Y., Ding, Y., Yang, W., Han, J., Jiang, S., and He, S. Nitrogen-doped carbon layer on cellulose derived free-standing carbon paper for high-rate supercapacitors. *Applied Surface Science*, *608*:155144, 2023.

[45] Wang, L., Wang, C., Wang, H., Jiao, X., Ouyang, Y., Xia, X., Lei, W., and Hao, Q. ZIF-8 nanocrystals derived N-doped carbon decorated graphene sheets for symmetric supercapacitors. *Electrochimica Acta*, *289*:494-502, 2018.

[46] Demarconnay, L., Raymundo-Piñero, E., and Béguin, F. A symmetric carbon/carbon supercapacitor operating at 1.6 V by using a neutral aqueous solution. *Electrochemistry Communications*, *12*(10):1275-1278, 2010.

[47] Hou, X., Ren, P., Dai, Z., Chen, H., Tang, W., Chen, Z., Ren, F., and Jin, Y. Ultrahigh voltage window, preeminent energy density aqueous supercapacitor derived from honeycomb-like porous carbon decorated with carbon dots. *Electrochimica Acta*, *425*:140336, 2022.

[48] An, Y., Li, Z., Yang, Y., Guo, B., Zhang, Z., Wu, H., and Hu, Z. Synthesis of Hierarchically Porous Nitrogen-Doped Carbon Nanosheets from Agaric for High-Performance Symmetric Supercapacitors. *Advanced Materials Interfaces*, *4*(12):1700033, 2017.

[49] Sahoo, M.K. and Rao, G.R. A high energy flexible symmetric supercapacitor fabricated using N-doped activated carbon derived from palm flowers. *Nanoscale Advances*, *3*(18):5417-5429, 2021.

[50] Zheng, L., Dai, X., Ouyang, Y., Chen, Y., and Wang, X. nHighly N/O co-doped carbon nanospheres for symmetric supercapacitors application with high specific energy. *Journal of Energy Storage*, *33*:102152, 2021.

[51] Wang, P., Zhang, G., Li, M.Y., Yin, Y.X., Li, J.Y., Li, G., Wang, W.P., Peng, W., Cao, F.F., and Guo, Y.G. Porous carbon for high-energy density symmetrical supercapacitor and lithium-ion hybrid electrochemical capacitors. *Chemical Engineering Journal*, *375*:122020, 2019.

[52] Manikandan, R., Raj, C.J., Moulton, S.E., Todorov, T.S., Yu, K.H., and Kim, B.C. High energy density heteroatom (O, N and S) enriched activated carbon for rational design of symmetric supercapacitors. *Chemistry–A European Journal*, *27*(2):669-682, 2021.

[53] Wang, Y., Liu, R., Tian, Y., Sun, Z., Huang, Z., Wu, X., and Li, B. Heteroatoms-doped hierarchical porous carbon derived from chitin for flexible all-solid-state symmetric supercapacitors. *Chemical Engineering Journal*, *384*:123263, 2020.

[54] Chen, L., Wen, Z., Chen, L., Wang, W., Ai, Q., Hou, G., Li, Y., Lou, J., and Ci, L. Nitrogen and sulfur co-doped porous carbon fibers film for flexible symmetric all-solid-state supercapacitors. *Carbon*, *158*:456-464, 2020.

[55] Liu, Z., Ai, J., Sun, M., Han, F., Li, Z., Peng, Q., Wang, Q.D., Liu, J., and Liu, L. Phosphorous-Doped Graphite Layers with Outstanding Electrocatalytic Activities for the Oxygen and Hydrogen Evolution Reactions in Water Electrolysis. *Advanced Functional Materials*, *30*(12):1910741, 2020.